RESEARCH ARTICLE

Evaluation of the Double Snap-Through Mechanism on the Wave Energy Converter's Performance

Bingqi Liu[1] · Carlos Levi[1] · Segen F. Estefen[1] · Zhijia Wu[2] · Menglan Duan[3]

Abstract

Lower efficiencies induce higher energy costs and pose a barrier to wave energy devices' commercial applications. Therefore, the efficiency enhancement of wave energy converters has received much attention in recent decades. The reported research presents the double snap-through mechanism applied to a hemispheric point absorber type wave energy converter (WEC) to improve the energy absorption performance. The double snap-through mechanism comprises four oblique springs mounted in an X-configuration. This provides the WEC with different dynamic stability behaviors depending on the particular geometric and physical parameters employed. The efficiency of these different WEC behaviors (linear, bistable, and tristable) was initially evaluated under the action of regular waves. The results for bistable or tristable responses indicated significant improvements in the WEC's energy capture efficiency. Furthermore, the WEC frequency bandwidth was shown to be significantly enlarged when the tristable mode was in operation. However, the corresponding tristable trajectory showed intra-well behavior in the middle potential well, which induced a more severe low-energy absorption when a small wave amplitude acted on the WEC compared to when the bistable WEC was employed. Nevertheless, positive effects were observed when appropriate initial conditions were imposed. The results also showed that for bistable or tristable responses, a suitable spring stiffness may cause the buoy to oscillate in high energy modes.

Keywords Wave energy converter · Point absorber · Double snap-through mechanism · Bistable dynamic behavior · Tristable dynamic behavior

Article Highlights

- The energy capture efficiency of the WEC has been significantly improved in bistable or tristable mode.
- The WEC frequency bandwidth is shown to be significantly enlarged in the tristable mode.
- Compared to the bistable WEC, the intra-well behavior in the middle potential well of the tristable WEC induced a more severe low-energy absorption under small wave amplitude excitations.
- Positive effects on the low-energy absorption problem were observed when appropriate initial conditions were imposed in tristable WEC.

✉ Segen F. Estefen
  segen@lts.coppe.ufrj.br

1   Ocean Engineering Department, COPPE, Federal University of Rio de Janeiro, Rio de Janeiro 21945-970, Brazil

2   China Ship Scientific Research Center, Wuxi 214082, China

3   College of Safety and Ocean Engineering, China University of Petroleum-Beijing, Beijing 102249, China

1 Introduction

The continual increase in energy consumption globally is estimated as 9954 Mtoe ≈ 115765 TWh in 2020 (Enerdata 2021), unpredictable oil and gas market fluctuations, and the accelerating pressure to reduce greenhouse gas emissions has resulted in significant pressure to increase the energy generation from renewable sources. In the last few decades, renewable energy has begun to play an increasingly significant role in replacing conventional sources. In this respect, wave energy can provide continually available high-density energy (estimated as 146 TWh/year) (Edenhofer et al. 2011), and it has thus become a competitive renewable energy source. Also, recent investigations have shown that upper-ocean warming, mainly due to anthropogenic global warming, has caused significant increases in ocean wave heights, and global wave energy has been increasing at around 0.4% annually since 1948 (Reguero et al. 2019).

The technological race to harvest wave energy has resulted in the design, construction, and testing of various wave energy

converters (WECs) since the early 1980s (Czech and Bauer 2012; Falcão 2010; Shadman et al. 2019). In relation to their geometry, WECs are usually classified as being either terminator, attenuator, or point absorber (PA) types (Al Shami et al. 2019). As the PA type is mechanically simple and requires lower capital and maintenance costs, it has attracted considerable attention from the wave energy technical community (Astariz and Iglesias 2015). PA types also have vertically symmetrical geometric features, which enable them to extract energy independently from the direction of the incoming wave (Budal and Falnes 1982). Relatively small bodies, such as those used in a typical PA design, are also more convenient for working in the arrays used in offshore wave energy farms, and they can even be easily integrated with offshore wind farms (Anvari-Moghaddam et al. 2020). Such combined characteristics indicate the potential for the PA-WEC to be commercialized for use in the electricity market, or as a complementary power supply for oil and gas offshore plants and other offshore facilities.

However, the PA-WEC has a small characteristic length (usually smaller than the local predominant wavelength), which means that its operational bandwidth is narrower than that of other WEC concepts (e.g., terminator and attenuator devices). Therefore, the WEC-PA can only extract a significant amount of energy from wave components within a reasonably narrow wave frequency resonant band. If the PA's natural frequency lies out of the predominant sea wave frequency range, it undergoes an abrupt drop in its conversion efficiency. Therefore, PA-WECs need to be either significantly enlarged or be operated out of their resonant conditions.

To overcome such disadvantages, and to enhance their energy absorption efficiency, some alternative approaches have been proposed. For example, one direct and straightforward approach aimed to optimize buoy geometry at a given deployment site (Goggins and Finnegan 2014; Shadman et al. 2018); however, the results showed limited efficiency gains. It is evident, therefore, that to increase the potential efficiency gains to adequate levels, alternative control strategies that adopt either passive or active techniques need to be incorporated into the PA design, and the following schemes have been proposed: complex conjugate control (Maria-Arenas et al. 2019), damping control (Garcia-Rosa et al. 2017; Jin et al. 2019; Rodríguez et al. 2019), latching control (Babarit and Clément 2006; Falcão 2008; Henriques et al. 2016), and model predictive control (MPC) (Andersen et al. 2015; Faedo et al. 2017; Li and Belmont 2014a, 2014b). However, of these, bidirectional damping reactive power increases the complexity of the Power Take Off (PTO) mechanism, which impacts heavily on the cost of the device, and the other control strategies require accurate and a priori predictions of the wave excitation force acting on the PA; these impose heavy burdens and are major obstacles for enabling practical use of the device.

In light of such practical difficulties, many investigations are now focusing on the use of non-reactive and passive-target approaches (Wu et al. 2018, 2019; Younesian and Alam 2017). By taking the well-succeeded solution adopted in the vibration isolation problem and vibration energy harvesting (Ramlan et al. 2010), the nonlinear stiffness system (NSS) has been attracted increasing attention as a promising feasible, efficient, and simple solution that enables wave energy conversion (Zhang et al. 2014; Zhang and Yang 2015).

The bistable system configuration, which is known as a "snap-through mechanism," is a classical NSS that provides a nonlinear restoring force through the unique configuration of certain mechanical compression components, such as springs, pneumatic actuators, buckling beams, and magnets (Wei and Jing 2017). It has bistable dynamic behavior that provides two statically stable states and one unstable state. If the excitation frequency is lower than the natural frequency of the device, the potential escaping phenomenon of the bistable behavior causes the vibration energy harvester to absorb significantly more energy (Harne 2017). In addition, its nonlinear stiffness characteristics effectively broaden the frequency response bandwidth, which is beneficial for harvesting in an irregular excitation environment (Daqaq et al. 2014).

In recent years, the NSS has been attracting attention from researchers investigating ocean wave energy conversion technology, mainly due to its ability to modulate natural frequencies, which shifts it into the local dominant frequency range of the ocean waves. In addition, its characteristic bandwidth enlargement could be particularly beneficial when dealing with the typical random behavior of real sea conditions.

However, currently only a few studies have discussed the implementation of NSS in a PA design, either numerically or experimentally. For example, Zhang et al. (2014) proposed a nonlinear snap-through Power Take Off (PTO) system consisting of two symmetrically oblique springs, see Figure 1a, which provided a bistable mechanism. The authors conducted an extensive analysis and comparison using both regular and irregular waves and found that nonlinear WEC captures relatively larger amounts of wave energy, even when using devices with small dimensions with small amplitude waves. In addition, Todalshaug (2015) patented a WEC with a negative stiffness mechanism that uses either mechanical springs or pneumatic cylinders. The pneumatic configuration, see Figure 1b, was then patented under the commercial name of "WaveSpring" and used in the CorPower buoy prototype (CorPower), and to validate this innovative concept, "WaveSpring" was successfully tested in a 1/16 scale model (Todalshaug et al. 2016). The experimental results showed that the WEC responded efficiently if tuned to work within the resonant range, and an increase in its frequency bandwidth was found. Prior dry testing and ocean deployment was then conducted using a 1/2 scale WEC to verify the promising characteristics of the "WaveSpring" industrial prototype performance.
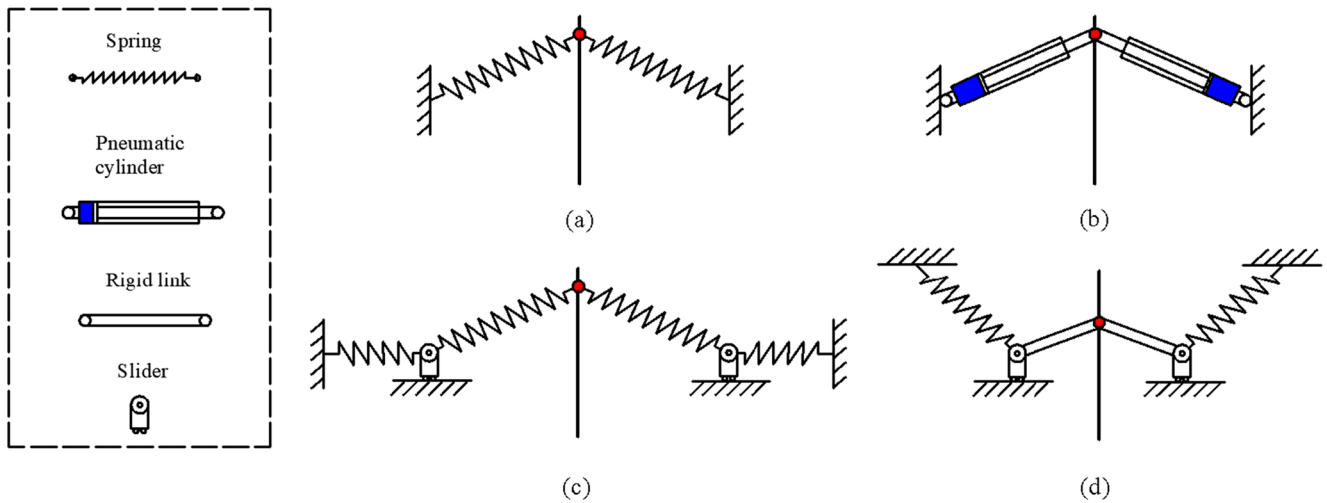
Figure 1 Schematic illustration of some of the nonlinear stiffness mechanisms previously proposed in literature: (**a**) conventional bistable mechanism, (**b**) pneumatic bistable mechanism, (**c**) adaptive bistable mechanism, and (**d**) multi-stable mechanism

In addition to the above-mentioned conventional bistable system, other nonlinear stiffness systems have been introduced into WEC technology. Zhang et al. (2018) proposed a novel adaptive bistable mechanism (see Figure 1c) that involves adopting two additional auxiliary springs for automatically adjusting the potential function for lowering the potential barrier near the unstable equilibrium position. The time-varying potential feature helps to avoid the possible occurrence of low-energy absorption, which can occur in the conventional bistable WEC. In addition, the adaptive bistable WEC can contain an even wider frequency bandwidth, if the right system parameters are selected. As an alternative to the conventional bistable potential adaptive, Younesian and Alam (2017) proposed a multi-stable mechanism composed of two oblique rigid links and two oblique springs (see Figure 1d) with additional potential wells introduced into the dynamic response. By adjusting the angle and initial spring lengths, the mechanical system can switch from monostable to bistable or tristable states, accordingly. Their results have shown that bistable and tristable modes significantly improve the WEC efficiency, and the natural frequency can be shifted to a higher frequency range. However, to achieve the tristable mode, the length of the rigid links needs to be at least three times the length of that of the initial spring, which means that it requires a larger operational space. In addition, the WEC responses and the effects of the system parameters in the tristable mode remain uncertain and have not been completely clarified.

Based on the above information, the present study introduces a simpler and more compact double snap-through mechanism that can be applied to work in a PA-WEC, enables the occurrence of multi-stable states, and requires only a relatively compact space. The main focus of this study is conducting a motion characteristic analysis. In addition, compared to previous studies mentioned above, greater insights into the wave amplitude effect are provided.

2 Point Absorber WEC (PA-WEC) Featuring a Double Snap-Through Mechanism

2.1 Description of Double Snap-Through Mechanism

Figure 2 shows a schematic diagram of the configuration of a WEC equipped with the proposed double snap-through mechanism. The hemispherical buoy is constrained to oscillate in heave motion only, and the PTO is placed on the seabed. The double snap-through mechanism comprises four oblique springs in an X-shaped layout. One end of each spring is connected to a seabed fixed support structure, and the other follows the buoy-PTO pole connector. A similar mechanism was proposed by Li et al. (2019), but its operations were limited to a bistable mode only. The present study investigates the full potential of the nonlinear stiffness mechanism in a
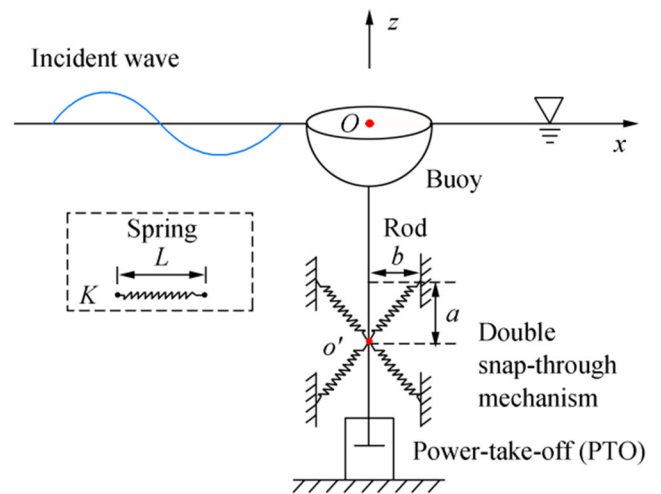
Figure 2 Schematic configuration of hemispherical point absorber with the proposed double snap-through mechanism

much broader perspective that includes an analysis of its tristable behavior.

In Figure 2, the vertical and horizontal distances between the spring fixed end supports are shown as $2a$ and $2b$, respectively, and the spring free length and stiffness are L and K, respectively.

For any given vertical displacement, z, at any instant, t, the vertical component of the force developed by the double snap-through mechanism can be given by

$$f_M = 2K(z+a)\left(1-\frac{L}{\sqrt{(z+a)^2+b^2}}\right) + 2K(z-a)\left(1-\frac{L}{\sqrt{(z-a)^2+b^2}}\right) \tag{1}$$

and the associate potential energy stored by the springs at any time, t, is

$$U = 2Kz^2 - 2KL\sqrt{(z+a)^2+b^2} \\ -2KL\sqrt{(z-a)^2+b^2} + 4KL\sqrt{a^2+b^2} \tag{2}$$

2.2 Mathematical Model

Applying the well-known Cummins equation (Cummins 1962), in the time domain, the governing equation of the hemispherical PA heave motion with double snap-through mechanism is given as follows:

$$(m+A_\infty)\ddot{z}(t) + \int_0^t K_I(t-\tau)\dot{z}(t)\mathrm{d}\tau + f_R(t) \\ = f_W(t) + f_{PTO}(t) \tag{3}$$

where $m = 2/3\pi R^3\rho$ is the buoy's physical mass; A_∞ is the buoy's added mass at an infinite frequency; ρ is the water density; R is the hemispherical buoy radius; $z(t)$, $\dot{z}(t)$, and $\ddot{z}(t)$ are the heave displacement, velocity, and acceleration at time, t, respectively; and $K_I(t)$ is an impulse response function defined in the kernel of the convolution term and in consideration of the fluid memory effect of the radiation force. In Ogilvie (1964), $K_I(t)$ relates to the radiation damping coefficient $B(\omega)$ as follows:

$$K_I(t) = \frac{2}{\pi}\int_0^\infty B(\omega)\cos(\omega t)\mathrm{d}t \tag{4}$$

Furthermore, $f_R(t)$ is the restoring force:

$$f_R(t) = C_{WL}z(t) + f_M(t) \tag{5}$$

where $C_{WL} = \rho g\pi R^2$ is the linear hydrostatic restoring coefficient, g is gravity, and $f_M(t)$ is the vertical component of the force induced by the double snap-through mechanism used as given by Eq. (1).

On the right hand side of Eq. (3), $f_W(t)$ represents the vertical wave excitation force acting on the buoy. For regular waves, at any given wave frequency, ω, and wave amplitude, A, the corresponding force at any time, t, can be expressed as (Falnes 2002):

$$f_W(t) = A\sqrt{\frac{2g^3\rho B(\omega)}{\omega^3}}\sin(\omega t) \tag{6}$$

By considering a linear damper PTO (with a damping coefficient C), the PTO force can be calculated by:

$$f_{PTO}(t) = -C\dot{z}(t) \tag{7}$$

To accelerate the computational processing time involved to solve Eq. (3), the convolution integral can be solved through the state space model defined below (Wu et al. 2018):

$$\dot{X} = A'\cdot X + B'\cdot v \tag{8}$$

$$\mu = C'\cdot X \tag{9}$$

where $X = [x_1, x_2, \cdots, x_n]^T$ is the nth order state vector; A', B', and C' are the constant state space matrices that are calculated through the frequency domain identification (FDI) method discussed in Pérez and Fossen (2008, 2009); v is the buoy vertical velocity; and μ is the convolution term.

Substituting Eqs. (8) and (9) into Eq. (3), the state space model of the complete system is established as:

$$\begin{bmatrix} \dot{X} \\ \dot{z} \\ \dot{v} \end{bmatrix} = \begin{bmatrix} A' & 0 & B' \\ 0 & 0 & 1 \\ -C' & \frac{-C_{WL}}{m+A_\infty} & \frac{-C}{m+A_\infty} \end{bmatrix}\cdot\begin{bmatrix} X \\ z \\ v \end{bmatrix} + \begin{bmatrix} 0 \\ 0 \\ \frac{f_W-f_M}{m+A_\infty} \end{bmatrix} \tag{10}$$

The power capture efficiency is represented by the capture width ratio as defined in Eq. (11) (Falnes 2002):

$$\Omega = \frac{P_m}{2RP_{wave}} \tag{11}$$

where P_m is the average absorbed power,

$$P_m = \frac{1}{T}\int_0^T \left(C\cdot\dot{z}(t)\right)\cdot\dot{z}(t)\mathrm{d}t \tag{12}$$

P_{wave} is the wave energy flux per meter of wave front,

$$P_{wave} = \frac{\rho g^2 A^2}{4\omega} \tag{13}$$

and the constant values ρ, g, and R are used to define the non-dimensional parameters described below:

$$a^* = a/L, b^* = b/L, K^* = K/C_{WL}, L^* = L/R, \\ z^* = z/R, \omega^* = \omega/\sqrt{g/R}, C^* = C/\left(m\sqrt{g/R}\right), \\ A_\infty^* = A_\infty/m, t^* = t/\sqrt{R/g}, \tau^* = \tau/\sqrt{R/g}, A^* = A/R, \\ B^*(\omega) = B(\omega)/(m\omega) = B(\omega)/\left(m\omega^*\sqrt{g/R}\right). \tag{14}$$

The hydrodynamic coefficients for the hemispherical buoy can be obtained as discussed by Hulme (1982). The added mass at an infinite frequency is equal to $A_\infty^* = 0.5$, and the non-dimensional radiation damping coefficient, B^*, is shown in Figure 3.

The solution can be obtained by applying the 4th order FDI to define the matrices A', B', and C' and the 4th order classical Runge-Kutta method to solve the resultant ordinary differential equations (ODE) expressed by Eq. (10).

2.3 Static Analysis of the Multi-stable Mechanism

Based on the shape of the potential energy curve, U, as expressed by Eq. (2), the dynamic behavior of the double snap-through mechanism can be classified into three categories according to the characteristics of the respective curves:

- Monostable, involving a single potential well with one stable equilibrium (one global minimum) (see Figure 4a)
- Bistable, involving a double potential well with two stable equilibria (two minima) and with one unstable equilibrium (one local maximum) in the middle (see Figure 4b)
- Tristable, involving a triple potential well with three stable equilibria (three local minima) separated by two unstable equilibria (two local maxima) (see Figure 4c)

To define the shapes of the bistable and tristable potential curves shown in Figure 4, four parameters are given as follows: Δz_{p1}^*, representing half of the displacement difference between two outer stable equilibria for the bistable and tristable modes; Δz_{p2}^*, representing half of the displacement difference between the two unstable equilibria for the tristable mode; and ΔU_{p1}^* and ΔU_{p2}^* representing the difference between the potential energy for stable and unstable equilibria.
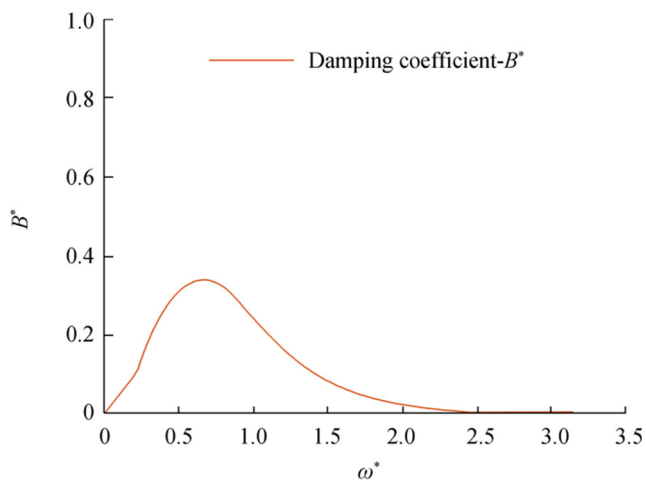
Figure 3 Non-dimensional radiation damping coefficient: hemispherical buoy in heave motion (Hulme 1982)

Also known as a potential barrier, this defines the threshold value for the escaping energy level (ΔU_{p1}^* for the bistable mode; ΔU_{p1}^*, ΔU_{p2}^* for the tristable mode).

Figure 5 presents a stability distribution diagram of the double snap-through mechanism. For a given combination of spring physical characteristics (K^*, L^*), there exists a specific combination of geometric parameters (a^*, b^*) that determine its stability characteristics. For instance, if we take the horizontal distance as $b^* = 0.4$, the system stability moves from bistable (orange region) to tristable (green region) then to monostable (red region), if a^* continues to increase.

The displacement difference and the potential barrier corresponding to the stable and unstable equilibria are two key factors used in the analysis of the device performance. Figure 6 presents the results for the displacement difference and potential barrier in the (a^*, b^*) domain. In this respect, Figure 6 a and b show that the (outer) stable equilibrium position, Δz_{p1}^*, and the (outer) potential barrier, ΔU_{p1}^*, increase as a^* and b^* decrease. For the middle potential well, as shown in Figure 6c, the unstable equilibrium position, Δz_{p2}^*, appears to have a greater relationship with a^*, while the potential barrier, ΔU_{p2}^*, shows the opposite tendency with respect to ΔU_{p1}^*.

Figure 7 shows the influence of spring stiffness, K^*, on the potential curve behavior. The curves shown in Figure 7 were obtained for a given set of geometrical parameters ($a^* = 0.4$, $b^* = 0.3$) to illustrate the tristable stability mode (triple potential well). The depth of the potential curve is seen to change when the spring stiffness, K^*, is adjusted. The results from Figure 7 show that with an increase in the value of K^*, the potential well depth becomes deeper, and this corresponds to higher potential barrier values.

3 Analysis of WEC Efficiency

An evaluation of the effect of employing the double snap-through mechanism on the operational of the WEC was conducted to compare its performance with the linear WEC. Figure 8 shows the power capture width ratio for the linear WEC in the (ω^*, C^*) parametric space. To enable the intuitive comparison discussed in the following sections, the upper limit of the capture width ratio of the color grading scale was set as $\Omega = 1.5$. Complying with the correct physics of the linear WEC, the numerical results clearly show that the maximum value of the capture width ratio occurs at a resonance frequency of $\omega^* = 1.0$. The optimal capture width ratio is $\Omega = 0.49$, and the corresponding operational conditions are defined by $C^* = 0.25$. A similar analysis is discussed in Zhang et al. (2018) and Zhang et al. (2019b).

For the 2.5 m radius hemisphere used here, the optimal conditions are $C^* = 0.25$ (corresponding to the damping

(a) Monostable   (b) Bistable   (c) Tristable
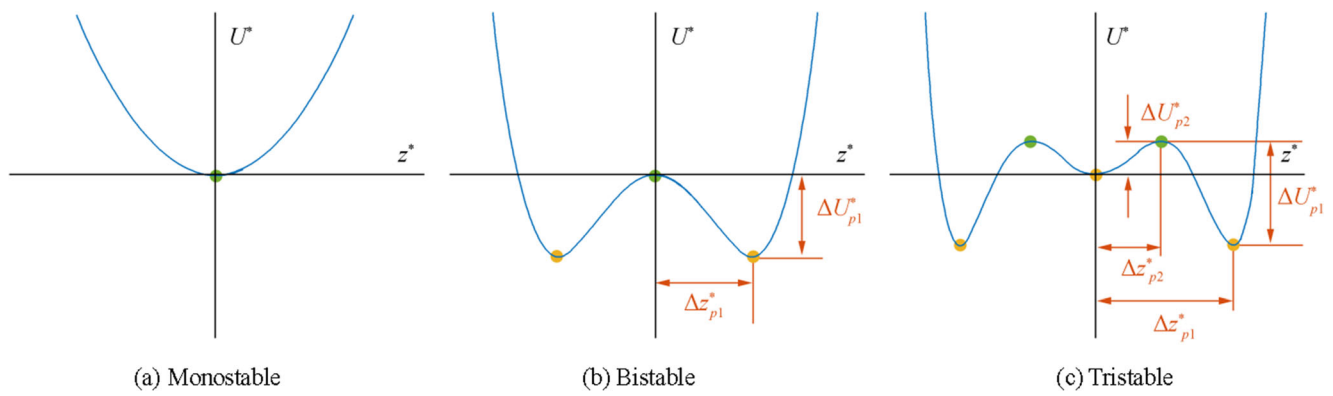
Figure 4 Potential energy curves: (**a**) monostable, (**b**) bistable, and (**c**) tristable

coefficient, $C = 16611$ kg/s) and the WEC natural period corresponding to 3.2 s ($\omega^* = 1.0$). As most of the ocean's energy is concentrated in waves lying within the period range of 5.0 s to 15.0 s ($\omega^* = 0.21$ to 0.63) (Falnes 2002), the linear WEC natural period ($\omega^* = 1.0$) is out of the energetic wave range, which results in a very poor performance.

The results obtained from the linear WEC performance were used to validate the numerical tools developed here, through a code-to-code verification strategy.

In the following sections, the discussion focuses on possible ways of applying the double snap-through mechanism to improve the WEC performance. In Section 3.1, the WEC motion characteristics resulting from the use of the double snap-through mechanism to induce bistable and tristable WEC modes generated data that are subsequently analyzed using time series, phase portrait, and frequency spectra. In Sections 3.2 to 3.5, parametric studies show the effects of varying wave and WEC parameters on its power capture performance.

3.1 WEC Motion Characteristics

To illustrate the performance of bistable and tristable WEC modes, the following set of parameters were selected in the
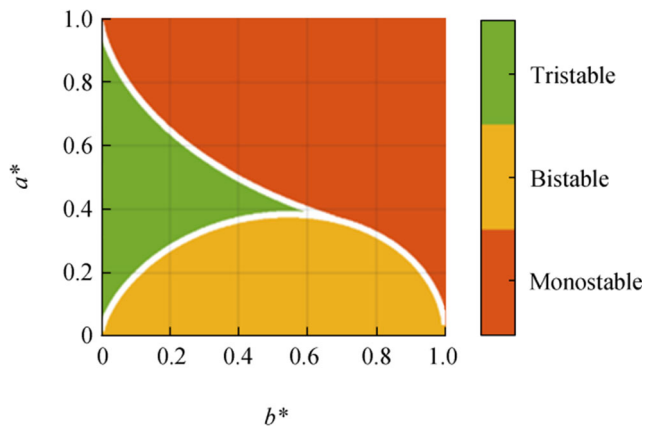
**Figure 5** Double snap-through mechanism: stability distribution regions ($K^* = 1.0$, $L^* = 1.0$)

following text: (a) $a^* = 0.30$, $b^* = 0.50$, $K^* = 1.0$, $L^* = 1.0$, $A^* = 0.20$, and $C^* = 0.25$, leading to a bistable mode, and (b) $a^* = 0.37$, $b^* = 0.37$, $K^* = 1.0$, $L^* = 1.0$, $A^* = 0.20$, and $C^* = 0.25$, leading to a tristable mode.

Figure 9 shows the capture width ratio as a function of the wave frequency for each one of the defined WEC modes. Different from the smooth and continuous linear WEC curve, the figure clearly shows that the bistable and tristable WEC curves are split into three distinct regions: the blue curve on the left (left branch), the blue curve on the right (right branch), and a set of randomly distributed points between the two branches (chaotic zone). The marked points P1-P5 were selected to illustrate the different possible responses of the double snap-through mechanism: P1 and P2 both lie on the left branch curves and show high inter-well motions (as described in Figure 10); P3 lies inside the chaotic zones and shows a chaotic motion (as described in Figure 11); P4 was defined for the bistable mode and it lies inside the chaotic zone; for the tristable mode, P4 lies on the right branch curve and indicates distinct responses for each mode; and P5 lies on the right branch curves and presents intra-well motions (as described in Figure 12).

Figure 9 shows that the maximum capture width ratio of both bistable and tristable WECs is $\Omega = 1.31$; this result is 267% greater than the maximum value of the linear WEC ($\Omega = 0.49$).

Further, the optimal wave frequencies for bistable ($\omega^* = 0.55$) and tristable ($\omega^* = 0.59$) are much lower than that for linear WEC ($\omega^* = 1.00$), and both of them are in the frequency range of typical high-energy ocean waves ($\omega^* = 0.21$ to 0.63).

Zhang et al. (2019a) defines the operational frequency bandwidth as the range in which the energy power capture ratio is greater than half of the linear WEC maximum value. Based on such a criterion, the results in Figure 9 show that the frequency bandwidths for linear, bistable, and tristable WECs are $\Delta\omega^* = 0.4$, 0.6, and 0.95, respectively. Therefore, the bistable and tristable WEC frequency bandwidths are 150% and 240% greater than the linear WEC range, which demonstrates their intrinsic ability to broaden the operational frequency bandwidth, particularly in the case of the tristable WEC.
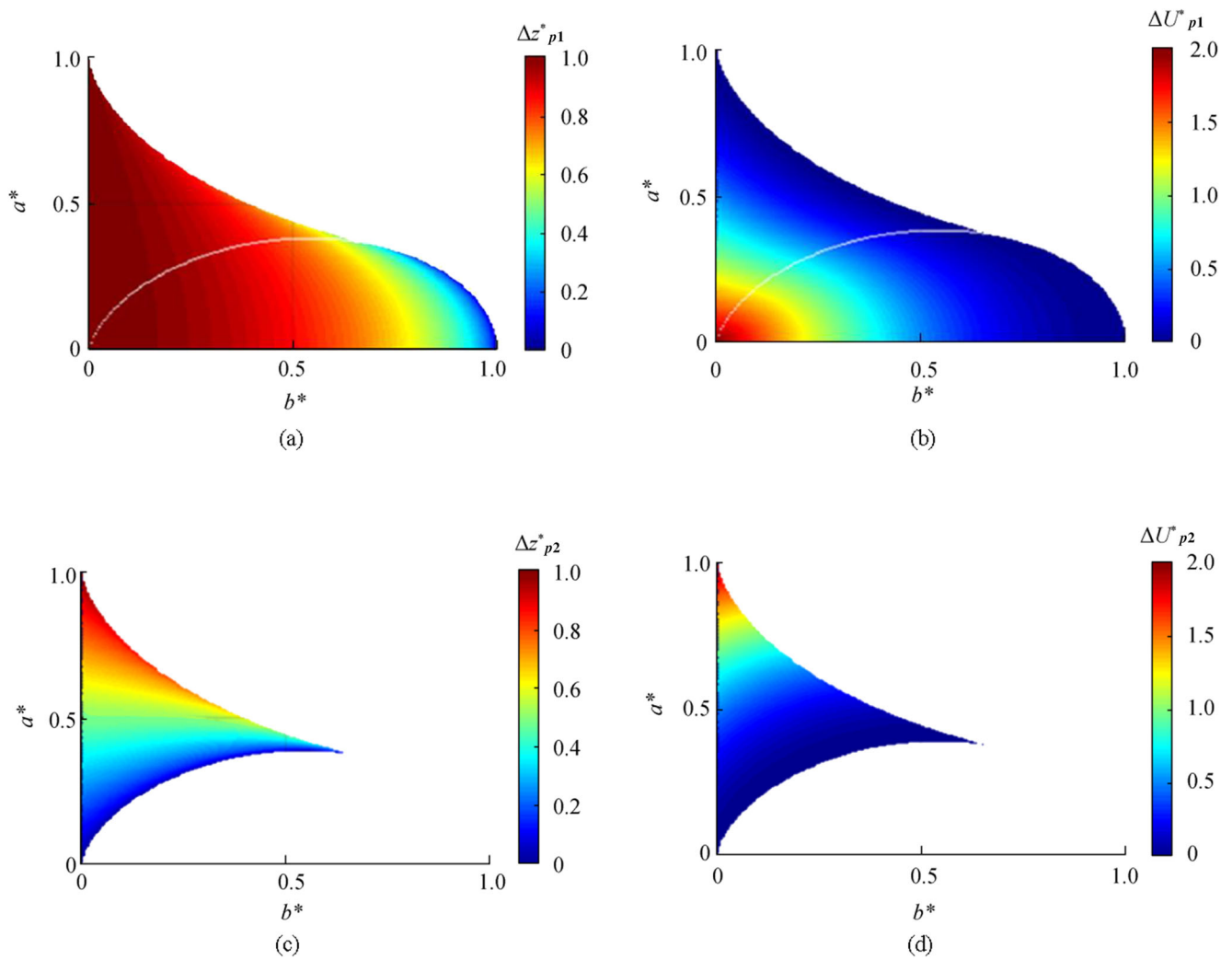
Figure 6 Stable and unstable equilibria ($K^* = 1.0$, $L^* = 1.0$): (**a**) bistable displacement difference (Δz_{p1}^*), (**b**) bistable potential barrier (ΔU_{p1}^*), (**c**) tristable displacement difference (Δz_{p2}^*), and (**d**) tristable potential barrier (ΔU_{p2}^*)
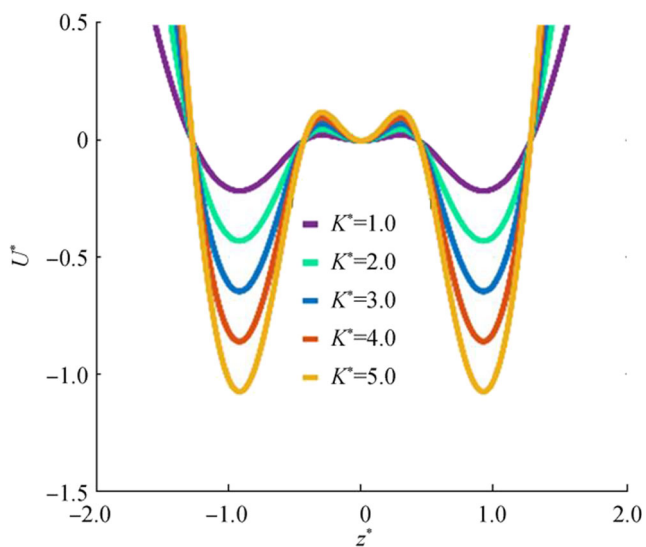
Figure 7 The effect of spring stiffness (K^*) on tristable potential curves ($a^* = 0.4$, $b^* = 0.3$, $K^* = 1.0$, $L^* = 1.0$)
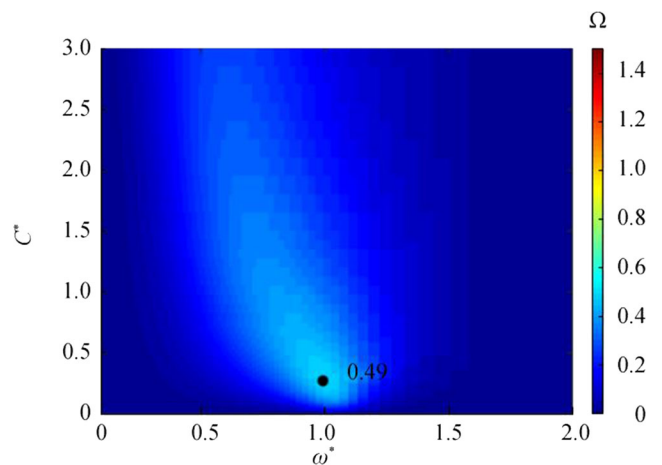
Figure 8 Energy capture width ratio: linear WEC in the (ω^*, C^*) parametric space
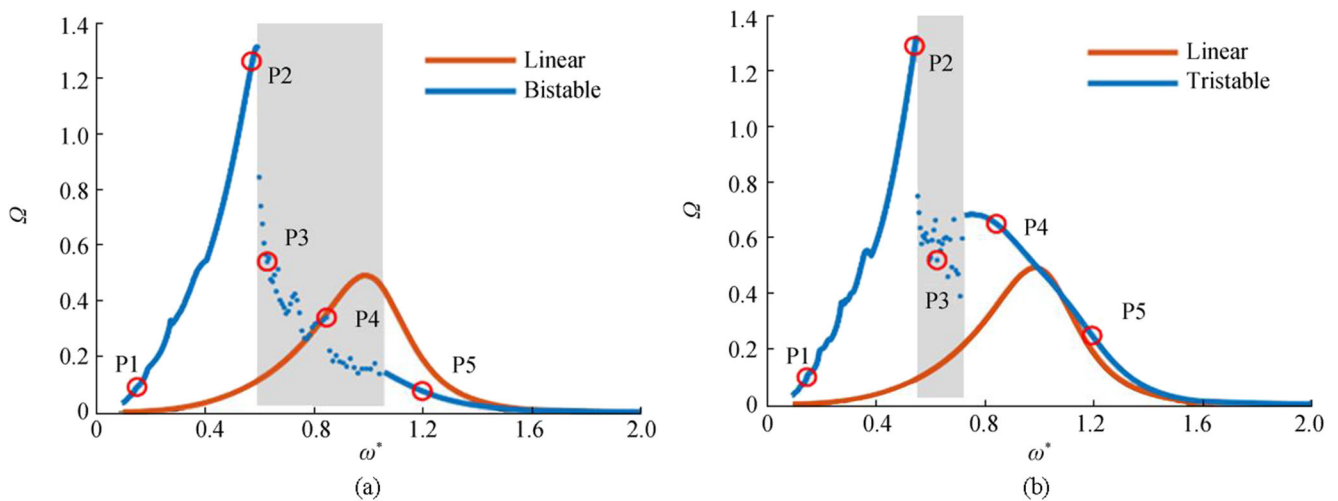
Figure 9 Wave energy capture width ratio versus wave frequency. (**a**) Bistable: $a^* = 0.30$, $b^* = 0.50$, $K^* = 1.0$, $L^* = 1.0$, $A^* = 0.20$, $C^* = 0.25$. (**b**) Tristable: $a^* = 0.37$, $b^* = 0.37$, $K^* = 1.0$, $L^* = 1.0$, $A^* = 0.20$, $C^* = 0.25$

Furthermore, Figure 9 a and b show that the left branches of both the bistable and tristable WEC provide consistently higher efficiencies than the linear WEC, thereby providing the much-needed efficiency enhancement. However, the right branch and chaotic zone of the bistable WEC (blue curve in Figure 9a) delivers a rather poorer performance and a more limited frequency bandwidth than the linear WEC responses (red curve in Figure 9a). With respect to the tristable WEC (blue curve in Figure 9b), if $\omega^* > 1.0$, the right branch of the tristable curve in Figure 9b (blue curve) shows that the operation of the tristable WEC is very close to that of the linear WEC (red curve), whereas if $0.75 < \omega^* < 1.0$ (left branch), the results show a superior performance for the tristable WEC, and thus great efficiency gain possibilities.

Solutions covering a given frequency range of incident waves acting on the linear, bistable, and tristable WEC responses illustrate the response behaviors corresponding to these three regions, and the underlying reasons for these are thus discussed.

The results in Figures 10, 11, and 12 show the heave displacement time history and the heave displacement phase and velocity phase portraits. The figures also include results of the spectral curves that were generated by a fast Fourier transform analysis of the corresponding time series.

Figure 10 shows the motion characteristics of the linear, bistable, and tristable modes for lower incident wave frequencies (i.e., P1: $\omega^* = 0.15$ and P2: $\omega^* = 0.55$). From Figure 10b–e, it is evident that the bistable and tristable mechanisms result in buoy responses that have larger amplitudes compared to the linear responses shown in Figure 10a, but they are nevertheless periodic. If $\omega^* = 0.15$ (Figure 10 b and d), the buoy oscillates either within one of the two potential wells (bistable) or in the two outer potential wells (tristable) several cycles prior to the snap-through behavior occurs, as previously indicated by Zhang et al. (2019a).

With respect to the latching control strategy, latching occurs if the buoy velocity is zero and releases it if the excitation wave force reaches its maximum value. Looking back at the response curves in Figure 10 b and d, the buoy was also trapped within the potential well, and it escaped when the maximum or minimum excitation forces occurred. This indicates that at low frequencies, the bistable and tristable mechanisms respond in the same way as those of the latch strategy. By increasing the incident wave frequency toward moderate values, such as $\omega^* = 0.55$ (as shown in Figure 10 c and e), larger amplitude periodic inter-well responses occur between the two potential wells, which means that the buoy reciprocates harmonically between the two equilibrium points.

However, with an increase in the wave frequency, the bistable and tristable WEC responses do not always manage to cross their corresponding potential barriers. In such cases, the WEC loses stability and oscillates chaotically around the potential wells. Such a behavior is observed in the results for P3 ($\omega^* = 0.61$) shown in Figure 11 b and c. The corresponding frequency spectra of the chaotic motions contain a wide range of frequency components, but they are still dominated by the incident wave frequency component.

If $\omega^* = 0.86$ (P4), the bistable WEC also oscillates in the chaotic zone and provides a low-energy output (see Figure 12b). However, with the tristable WEC, one single

Figure 10 WEC motion characteristics ($\omega^* = 0.15$ and 0.55): (**a**) linear, ▶ (**b**) bistable, (**c**) bistable, (**d**) tristable, and (**e**) Tristable. Non-dimensional variables as defined in Eq. (14): t^* is time, z^* is heave displacement, ω^* is the incident wave frequency, A_z^* is heave amplitude, and $v^* = dz^*/dt^*$ is heave velocity
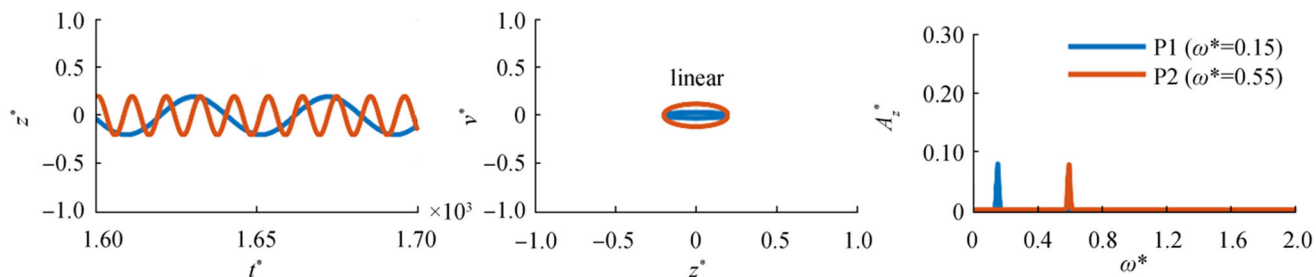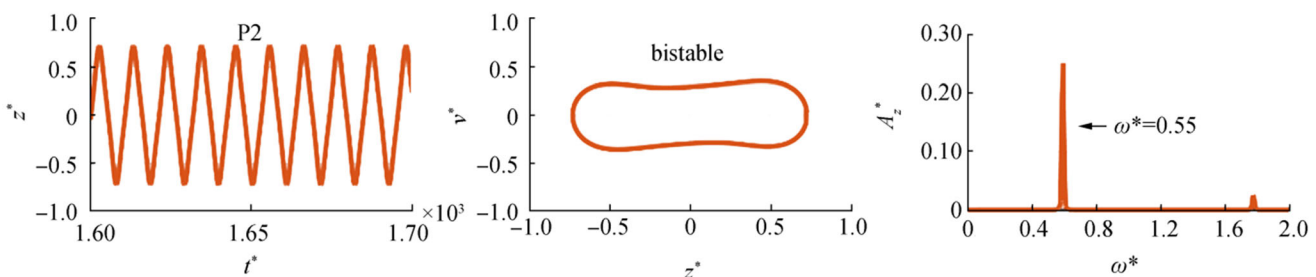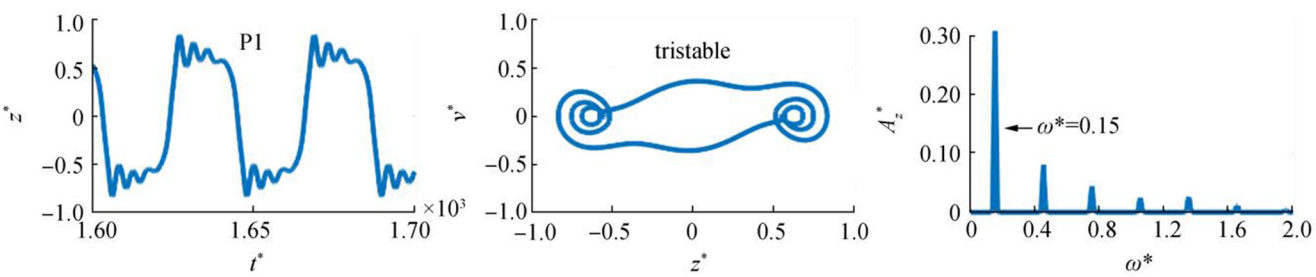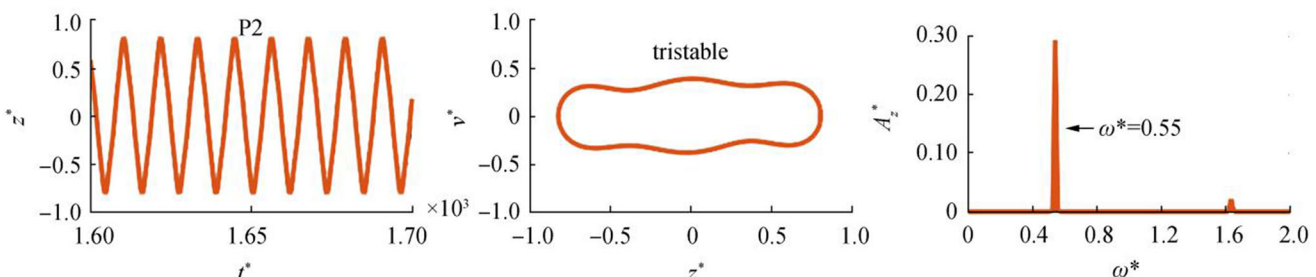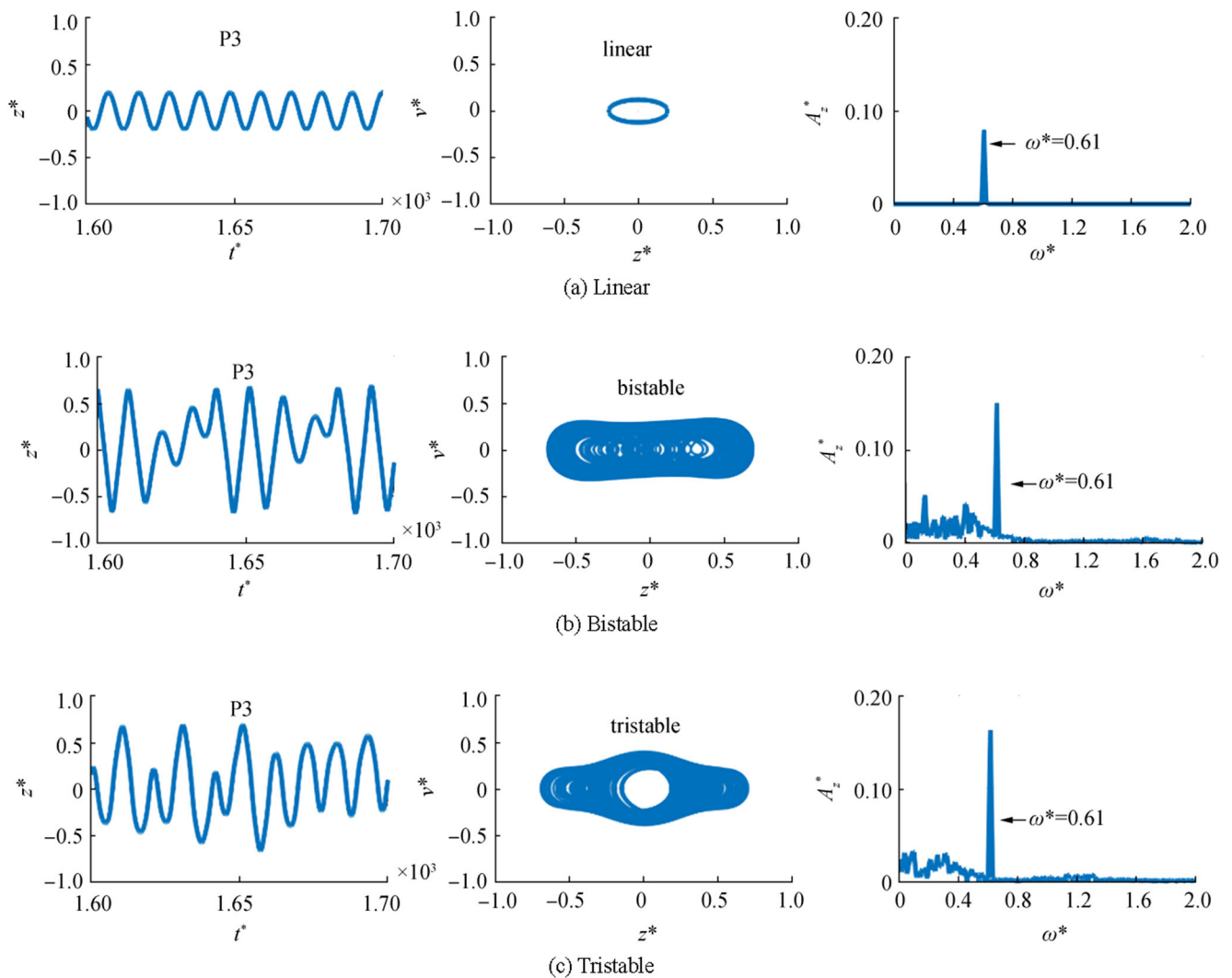
(a) Linear
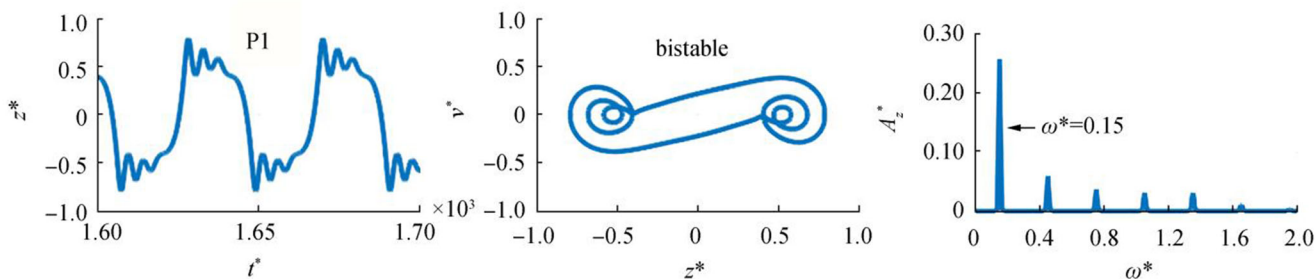
(b) Bistable

(c) Bistable

(d) Tristable

(e) Tristable

Figure 11 WEC motion characteristics ($\omega^* = 0.61$): (**a**) linear, (**b**) bistable, and (**c**) bistable

inter-well oscillation mode occurs around the middle potential well, and a relatively higher energy capture width ratio then develops, which provides evidence of the benefit of introducing an extra potential well. For a relatively higher wave frequency (P5: $\omega^* = 1.22$), the buoy does not cross the potential barrier, and it becomes trapped in one of the potential wells with a periodic intra-well oscillation (see Figure 12 d and e).

3.2 Effect of PTO Damping

Figure 13 shows a 2D color plot of the wave energy capture width ratio in the (ω^*, C^*) domain. The upper limit of the color scale is the same as that used in Figure 8 ($\Omega = 1.5$). It is evident that the optimal operational conditions for the bistable mode are $\omega^* = 0.56$ and $C^* = 0.33$, while the optimal operational conditions for the tristable mode are $\omega^* = 0.53$ and $C^* = 0.36$. A comparison with the linear WEC (see Figure 8) shows that the bistable and tristable responses reach higher efficiencies (much higher than the optimal value of the linear

WEC: $\Omega = 0.49$) in a broader wave frequency bandwidth and a larger PTO damping range. However, if the PTO damping parameter (C^*) is increased, the optimal capture width ratio firstly increases, reaches its maximum, and then begins to decrease. In addition, the optimal operation frequency shifts to lower values.

The white dashed line in Figure 13 corresponds with the bistable and tristable WEC bifurcation diagram shown in Figure 9 ($C^* = 0.25$). For the bistable WEC (see Figure 13a), the high efficiency (red) region relates to the left branch, and a sharp drop is then seen when moving toward the chaotic zone and the right branch. In contrast with the bistable response, there is no sharp drop transition in the tristable response, and a significantly high energy capture width ratio occurs over a broader region in relation to the superior performance defined by the right branch. This result proves that an extra potential well (the middle potential well) can enlarge the response frequency bandwidth.
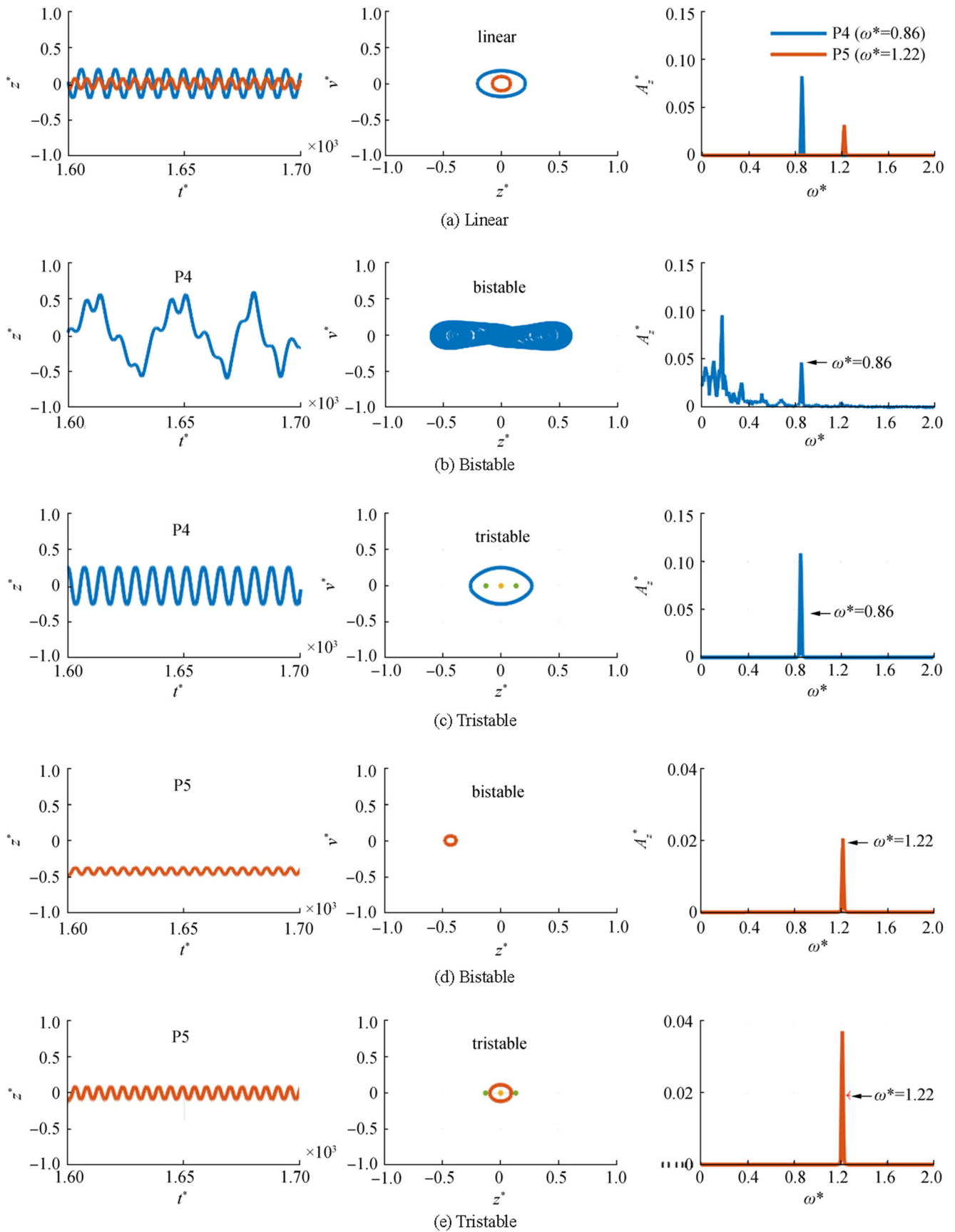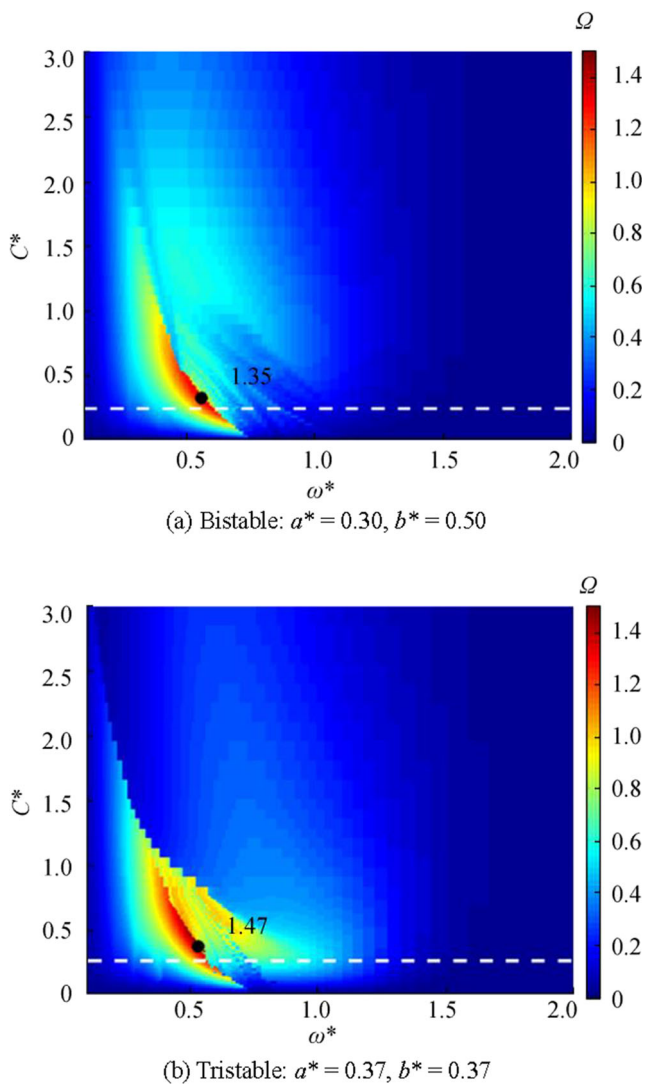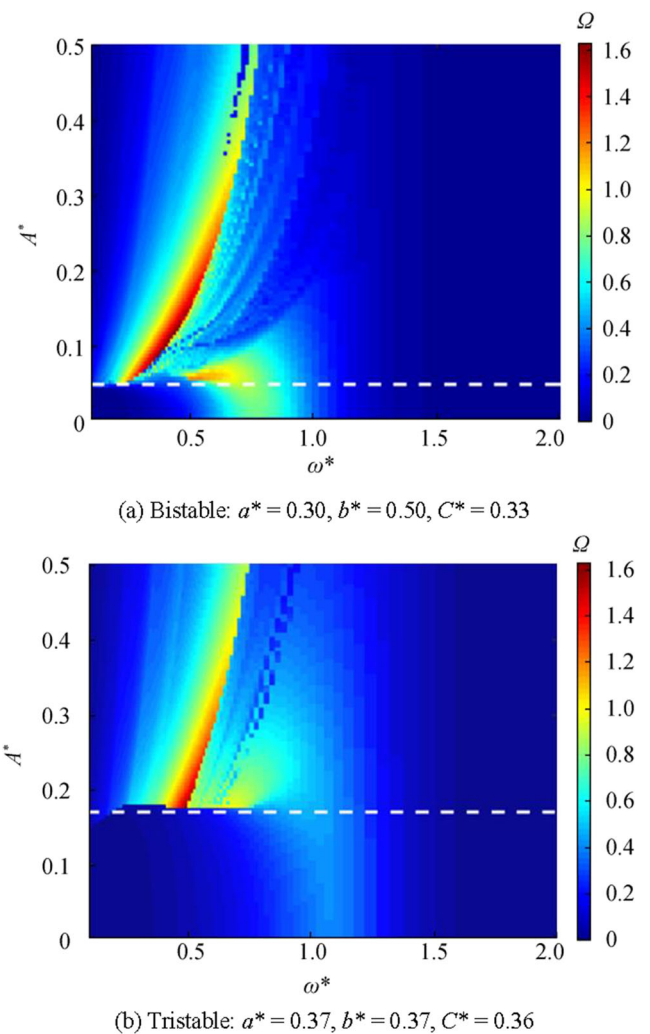
Figure 12 WEC motion characteristics ($\omega^* = 0.86$ and 1.22): (**a**) linear, (**b**) bistable, (**c**) tristable, (**d**) bistable, and (**e**) tristable

(a) Bistable: $a^* = 0.30$, $b^* = 0.50$

(b) Tristable: $a^* = 0.37$, $b^* = 0.37$

Figure 13 Wave energy capture width ratio in (ω^*, C^*) domain ($K^* = 1.0$, $L^* = 1.0$, $A^* = 0.2$). (**a**) Bistable: $a^* = 0.30$, $b^* = 0.50$. (**b**) Tristable: $a^* = 0.37$, $b^* = 0.37$

(a) Bistable: $a^* = 0.30$, $b^* = 0.50$, $C^* = 0.33$

(b) Tristable: $a^* = 0.37$, $b^* = 0.37$, $C^* = 0.36$

Figure 14 Wave energy capture width ratio in (ω^*, A^*) domain ($K^* = 1.0$, $L^* = 1.0$). (**a**) Bistable: $a^* = 0.30$, $b^* = 0.50$, $C^* = 0.33$. (**b**) Tristable: $a^* = 0.37$, $b^* = 0.37$, $C^* = 0.36$

3.3 Effect of Wave Amplitude

Figure 14 illustrates the variation in the wave energy capture width ratio as a function of the wave amplitude and frequency for both bistable and tristable responses. The optimal PTO damping obtained through the results presented in Figure 13 (i.e., $C^* = 0.33$, for bistable and $C^* = 0.36$, for tristable) was employed for the analysis of the influence of the wave amplitude discussed in this section. During displacements of the buoy with large amplitudes, the negative stiffness in both the bistable and the tristable responses has relatively little influence. Therefore, as shown in Figure 14a for the bistable and Figure 14b for the tristable cases, the peak energy capture width ratio decreases as the wave amplitude increases. Also, as shown in Figure 14a, the bistable WEC response captures only a small amount of energy when the wave amplitude is small ($A^* < 0.05$) (in Figure 14, represented by the regions

below the white dashed line). This low-energy-absorption limitation under low amplitude excitation conditions was previously observed, and is mentioned in. The physical reasoning is that the small amount of energy carried by the small amplitude waves is not sufficient to enable the buoy to cross the potential barrier. This traps the buoy either within one of the bistable potential wells or within the middle potential well in the tristable case. In Figure 14b, which shows the results for the tristable WEC, the low-energy-absorption limitation is even more evident. The capture width ratio shows a very sharp drop when a decrease in the wave amplitude occurs ($A^* < 0.17$) (represented by the region below the white dashed line), and the buoy is trapped within the middle potential well.

In the above analysis, it is of note that the initial condition (initial displacement, z_0^*, and initial velocity, v_0^*) of the spring joint point (referred to as point O' in Figure 1) is zero for both the bistable and tristable WECs (i.e., $z_0^* = 0$ and $v_0^* = 0$). Therefore, different initial conditions were considered to

(a) Bistable: $A^* = 0.04$
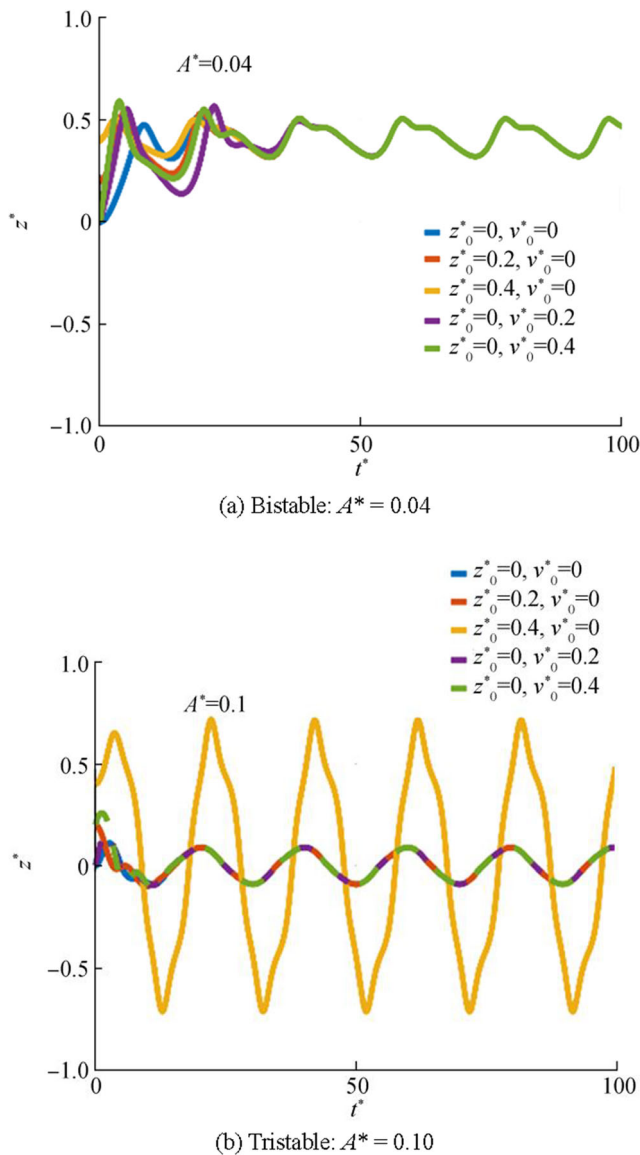
(b) Tristable: $A^* = 0.10$

Figure 15 Heave time history for different initial conditions. (**a**) Bistable: $A^* = 0.04$. (**b**) Tristable: $A^* = 0.10$

investigate their effect on the responses of bistable and tristable WECs. Figure 15 a presents the results for the bistable WEC under different combinations of initial conditions at a small wave amplitude ($A^* = 0.04$), represented by the region below the white dashed line in Figure 14a. Although the initial conditions produce different responses in the transient phase, the buoy displacement stabilizes after a few cycles, which indicates that the initial conditions have a minimal effect on the response.

For the tristable WEC, the selected wave amplitude corresponds to $A^* = 0.10$. The results shown in Figure 15b indicate that if the initial conditions are defined by $z_0^* = 0.4$ and $v_0^* = 0$, the buoy overpasses the potential barriers and reaches a high amplitude inter-well oscillation. However, other initial conditions can trap the buoy within the middle potential well, leading to small amplitude intra-well oscillations.

Figure 16 illustrates the energy capture width ratio in the (ω^*, A^*) domain for the tristable WEC with initial conditions defined by $z_0^* = 0.4$ and $v_0^* = 0$. A comparison with the tristable WEC performance with zero initial conditions (see Figure 14(b)) shows that the efficiency in the region below the white dashed line is greatly enhanced and the low-energy-absorption limitation is significantly alleviated. In addition, there is limited change in the region above the white dashed line, which shows no change in the energy capture width ratio, and there is thus no detrimental effect on the tristable WEC's performance.

3.4 Effect of Spring End Positions

As described in Section 2.3, the combined parameters, a^* and b^*, which define the spring end positions, determine whether the system operates in a monostable, bistable, or tristable mode. Two different waves (i.e., $\omega^* = 0.53$, $A^* = 0.2$ and $\omega^* = 0.53$, $A^* = 0.5$) were chosen to investigate the influence of geometry on the WEC's performance, and the corresponding results are shown in Figure 17.

The results indicate the WEC efficiency can be significantly improved in both the bistable and tristable modes when a suitable (a^*, b^*) combination is employed, whereas the use of the monostable WEC always leads always to a poorer efficiency.

In addition, the efficiency of the tristable WEC under relatively higher amplitude conditions (see Figure 17b) is superior to that of the bistable WEC. Furthermore, compared with the results shown Figure 6, the high-efficiency region in Figure 17 features a similar trend for both the displacement difference and the potential barrier, which implies that these two factors co-determine the WEC's performance under certain external excitations.
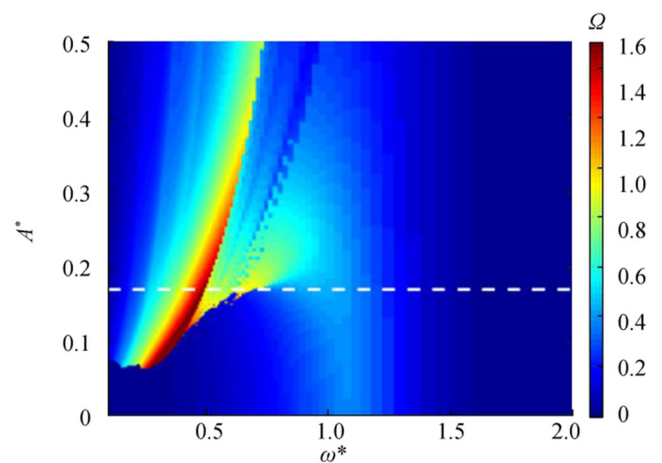
Figure 16 Wave energy capture width ratio: tristable in (ω^*, A^*) domain with initial conditions ($z_0^* = 0.4$, $v_0^* = 0$)
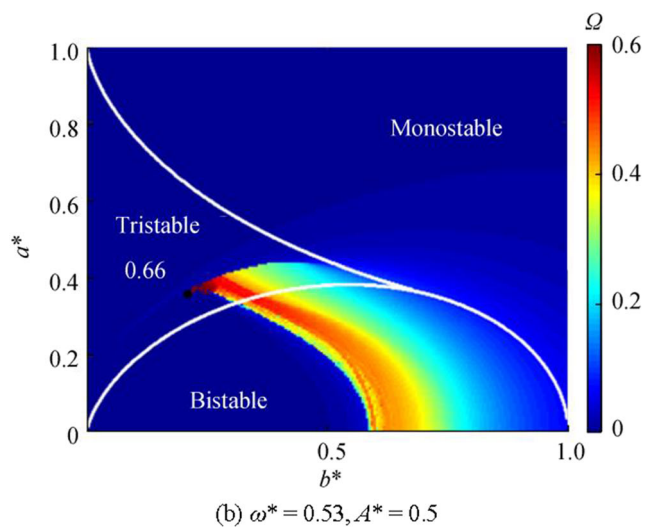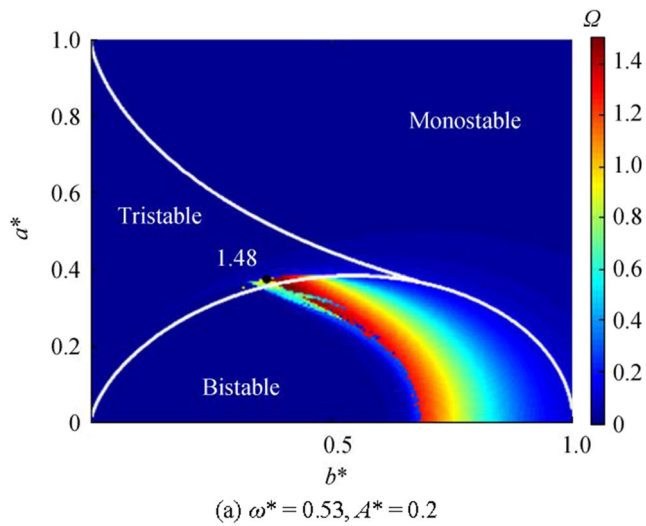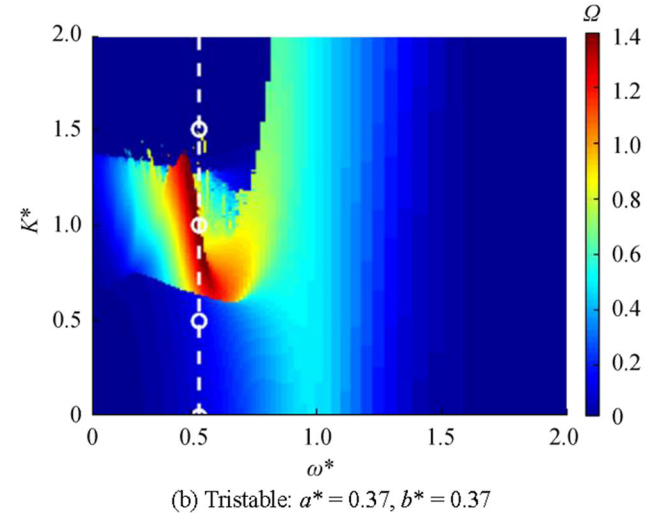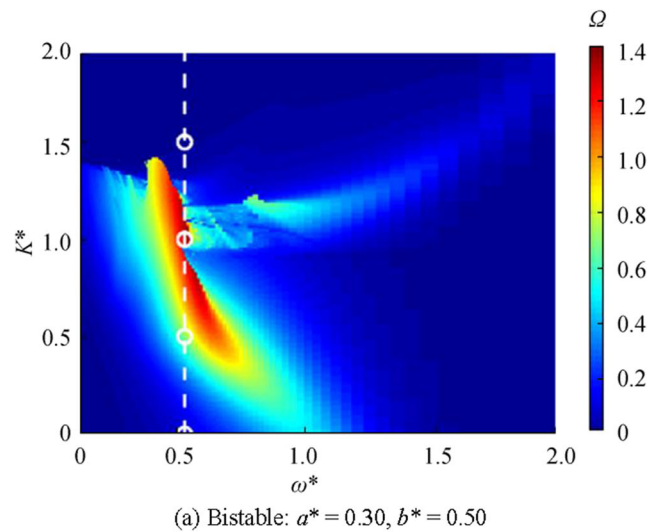
(a) $\omega^* = 0.53, A^* = 0.2$

(b) $\omega^* = 0.53, A^* = 0.5$

Figure 17 Wave energy capture width ratio in the (a^*, b^*) domain ($C^* = 0.36$, $K^* = 1.0$, $L^* = 1.0$). (**a**) $\omega^* = 0.53$, $A^* = 0.2$. (**b**) $\omega^* = 0.53$, $A^* = 0.5$

(a) Bistable: $a^* = 0.30, b^* = 0.50$

(b) Tristable: $a^* = 0.37, b^* = 0.37$

Figure 18 Wave energy capture width ratio in (ω^*, K^*) domain ($C^* = 0.36$, $L^* = 1.0$, $A^* = 0.2$). (**a**) Bistable: $a^* = 0.30$, $b^* = 0.50$. (**b**) Tristable: $a^* = 0.37$, $b^* = 0.37$

3.5 Effect of Spring Stiffness

Figure 7 showed that spring stiffness, K^*, affects the intensity of the depth of the potential curve associated with the double snap-through mechanism. Further analysis is conducted in this section to discuss the influence of spring stiffness on the wave energy capture width ratio using the results presented in Figure 18.

These results show a significant improvement in the WEC efficiency that is obtained when a suitable K^* range is employed. For a small spring stiffness (i.e., $K^* = 0.5$), the potential curve depth is shallower, and this corresponds with the minor negative stiffness introduced by the double snap-through mechanism. As a result, the buoy trajectory (see blue curve in Figure 19) follows an elliptical shape that is similar to that of the linear WEC ($K^* = 0$). However, when a suitable spring stiffness is used (i.e., $K^* = 1.0$), the buoy can cross the potential barrier(s) and oscillate along a trajectory that has

reasonably high energy. If the spring stiffness is too high (i.e., $K^* = 2.0$), the threshold of the potential barrier becomes too large, and the buoy easily becomes trapped and forms a small amplitude oscillation within a single potential well.

4 Conclusions

This study applied a double snap-through mechanism to a hemispherical point absorber wave energy converter (PA-WEC) to evaluate the potential enhancement of its energy absorption efficiency. The practical configuration devised for the mechanism featured four symmetrical oblique springs with an X-shape layout.

By adjusting the PA's geometric and physical parameters, different multi-stable WEC dynamic behaviors were obtained. A general mathematical formulation based on non-dimensional parameters was used to calculate the time history
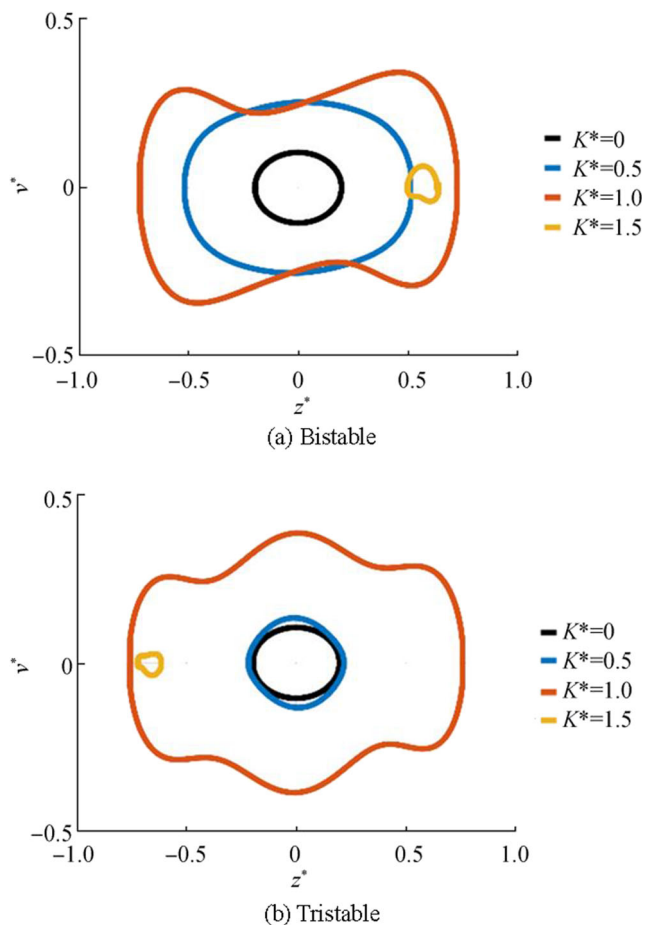
Figure 19 Phase portrait for selected configurations from Figure 18: (**a**) bistable and (**b**) tristable

WEC, such a limitation may be attenuated by imposing appropriate initial conditions.

4) The geometric parameters (i.e., $a*$ and $b*$) determine the dynamic characteristics of the system and invoke the use of either monostable, bistable, or tristable modes.

5) A large spring stiffness may cause the buoy to operate in one potential well, and a small spring stiffness can cause linear behavior. However, a suitable spring stiffness enables the buoy to oscillate within a reasonably high energy trajectory.

of the response for the multi-stable systems operating in regular waves. An analysis of the results included extensive comparisons between the performances of linear, bistable, and tristable WEC modes and included an evaluation of the influence of certain practical parameters on the WEC energy capture width ratio.

Based on the above-mentioned analysis, the main conclusions are listed as follows:

1) The double snap-through mechanism may cause the WEC to undergo both bistable and tristable dynamic behaviors, depending on the suitable combination of relevant parameters. The resulting effect may significantly improve the energy capture efficiency of the system.

2) Compared with the bistable WEC, the tristable WEC features a broader frequency bandwidth, which is associated with the presence of the middle potential well.

3) A limitation of the WEC's efficiency was identified in relation to the possible occurrence of low-energy absorption under small wave amplitude excitations. This occurred with the bistable WEC, and it was even more obvious for the tristable WEC. However, for the tristable

References

Al Shami E, Zhang R, Wang X (2019) Point absorber wave energy harvesters: a review of recent developments. Energies 12(1):47. https://doi.org/10.3390/en12010047

Andersen P, Pedersen TS, Nielsen KM, Vidal E, (2015). Model predictive control of a wave energy converter. *2015 IEEE Conf. Control Appl. CCA 2015 - Proc*, Sydney, 1540–1545. https://doi.org/10.1109/CCA.2015.7320829

Anvari-Moghaddam A, Mohammadi-Ivatloo B, Asadi S, Larsen KG, Shahidehpour M (2020) Sustainable energy systems planning, integration, and management. Applied Sciences, Switzerland. MDPI. https://doi.org/10.3390/app9204451

Astariz S, Iglesias G (2015) The economics of wave energy: a review. Renew Sust Energ Rev 45:397–408. https://doi.org/10.1016/j.rser.2015.01.061

Babarit A, Clément AH (2006) Optimal latching control of a wave energy device in regular and irregular waves. Appl Ocean Res 28(2):77–91. https://doi.org/10.1016/j.apor.2006.05.002

Budal K, Falnes J (1982) Wave power conversion by point absorbers: a Norwegian project. Int J Ambient Energy 3:59–67. https://doi.org/10.1080/01430750.1982.9675829

Cummins WE (1962) *The impulse response function and ship motions.* Navy Dep, David Taylor Model Basin

Czech B, Bauer P (2012) Wave energy converter concepts: design challenges and classification. IEEE Ind Electron Mag 6:4–16. https://doi.org/10.1109/MIE.2012.2193290

Daqaq MF, Masana R, Erturk A, Quinn DD (2014) On the role of non-linearities in vibratory energy harvesting: a critical review and discussion. Appl Mech Rev 66(4):040801. https://doi.org/10.1115/1.4026278

Edenhofer O, Madruga RP, Sokona Y, Seyboth K, Matschoss P, Kadner S, Zwickel T, Eickemeier P, Hansen G, Schlömer S, von Stechow C (2011) Renewable energy sources and climate change mitigation: special report of the intergovernmental panel on climate change. Cambridge University Press, Cambridge, United Kingdom. https://doi.org/10.1017/CBO9781139151153

Enerdata (2021) EnerOutlook 2050. Available from https://eneroutlook.enerdata.net/. Accessed 4 Mar 2021

Faedo N, Olaya S, Ringwood JV (2017) Optimal control, MPC and MPC-like algorithms for wave energy systems: an overview. IFAC J Syst Control 1:37–56. https://doi.org/10.1016/j.ifacsc.2017.07.001

Falcão AFDO (2008) Phase control through load control of oscillating-body wave energy converters with hydraulic PTO system. Ocean Eng 35(3-4):358–366. https://doi.org/10.1016/j.oceaneng.2007.10.005

Falcão AFDO (2010) Wave energy utilization: a review of the technologies. Renew Sust Energ Rev 14(3):899–918. https://doi.org/10.1016/j.rser.2009.11.003

Falnes J (2002) Ocean waves and oscillating systems: linear interactions including wave-energy extraction. Cambridge University Press, Cambridge

Garcia-Rosa PB, Kulia G, Ringwood JV, Molinas M (2017) Real-time passive control of wave energy converters using the Hilbert-Huang transform. IFAC-PapersOnLine 50(1):14705–14710. https://doi.org/10.1016/j.ifacol.2017.08.2502

Goggins J, Finnegan W (2014) Shape optimisation of floating wave energy converters for a specified wave energy spectrum. Renew Energy 71:208–220. https://doi.org/10.1016/j.renene.2014.05.022

Harne RLKWW (2017) Harnessing bistable structural dynamics: for vibration control, energy harvesting and sensing. Wiley

Henriques JCC, Gato LMC, Falcão AFO, Robles E, Faÿ FX (2016) Latching control of a floating oscillating-water-column wave energy converter. Renew Energy 90:229–241. https://doi.org/10.1016/j.renene.2015.12.065

Hulme A (1982) The wave forces acting on a floating hemisphere undergoing forced periodic oscillations. J Fluid Mech 121:443–463. https://doi.org/10.1017/S0022112082001980

Jin S, Patton RJ, Guo B (2019) Enhancement of wave energy absorption efficiency via geometry and power take-off damping tuning. Energy 169:819–832. https://doi.org/10.1016/j.energy.2018.12.074

Li G, Belmont MR (2014a) Model predictive control of sea wave energy converters - Part I: A convex approach for the case of a single device. Renew Energy 69:453–463. https://doi.org/10.1016/j.renene.2014.03.070

Li G, Belmont MR (2014b) Model predictive control of sea wave energy converters - Part II: The case of an array of devices. Renew Energy 68:540–549. https://doi.org/10.1016/j.renene.2014.02.028

Li L, Zhang X, Yuan Z, Gao Y (2019) Multi-stable mechanism of an oscillating-body wave energy converter. IEEE Trans Sustain Energy 11(1):500–508. https://doi.org/10.1109/tste.2019.2896991

Maria-Arenas A, Garrido AJ, Rusu E, Garrido I (2019) Control strategies applied to wave energy converters: State of the art. Energies 12(16). https://doi.org/10.3390/en12163115

Ogilvie TF (1964) Recent progress toward the understanding and prediction of ship motions. *Proceedings of the 5th Symposium on Naval Hydrodynamics*, Bergen, Norway

Pérez T, Fossen TI (2008) Time-vs. frequency-domain identification of parametric radiation force models for marine structures at zero speed. Model. Identif. Control 29(1):1–19. https://doi.org/10.4173/mic.2008.1.1

Pérez T, Fossen TI (2009) A Matlab toolbox for parametric identification of radiation-force models of ships and offshore structures. Model Identif Control 30(1):1–15. https://doi.org/10.4173/mic.2009.1.1

Ramlan R, Brennan MJ, MacE BR, Kovacic I (2010) Potential benefits of a non-linear stiffness in an energy harvesting device. Nonlinear Dyn 59:545–558. https://doi.org/10.1007/s11071-009-9561-5

Reguero BG, Losada IJ, Méndez FJ (2019) A recent increase in global wave power as a consequence of oceanic warming. Nat Commun 10:1–14. https://doi.org/10.1038/s41467-018-08066-0

Rodríguez CA, Rosa-Santos P, Taveira-Pinto F (2019) Assessment of damping coefficients of power take-off systems of wave energy converters: a hybrid approach. Energy 169:1022–1038. https://doi.org/10.1016/j.energy.2018.12.081

Shadman M, Estefen SF, Rodriguez CA, Nogueira ICM (2018) A geometrical optimization method applied to a heaving point absorber wave energy converter. Renew Energy 115:533–546. https://doi.org/10.1016/j.renene.2017.08.055

Shadman M, Silva C, Faller D, Wu Z, de Freitas Assad LP, Landau L, Levi C, Estefen SF (2019) Ocean renewable energy potential, technology, and deployments: a case study of Brazil. Energies 12(19):3658. https://doi.org/10.3390/en12193658

Todalshaug JH (2015) Wave energy converter. International Patent WO 2015/107158 Al

Todalshaug JH, Ásgeirsson GS, Hjálmarsson E, Maillet J, Möller P, Pires P, Guérinel M, Lopes M (2016) Tank testing of an inherently phase-controlled wave energy converter. Int J Mar Energy 15:68–84. https://doi.org/10.1016/j.ijome.2016.04.007

Wei C, Jing X (2017) A comprehensive review on vibration energy harvesting: modelling and realization. Renew Sust Energ Rev 74:1–18. https://doi.org/10.1016/j.rser.2017.01.073

Wu Z, Levi C, Estefen SF (2018) Wave energy harvesting using nonlinear stiffness system. Appl Ocean Res 74:102–116. https://doi.org/10.1016/j.apor.2018.02.009

Wu Z, Levi C, Estefen SF (2019) Practical considerations on nonlinear stiffness system for wave energy converter. Appl Ocean Res 92:101935. https://doi.org/10.1016/j.apor.2019.101935

Younesian D, Alam MR (2017) Multi-stable mechanisms for high-efficiency and broadband ocean wave energy harvesting. Appl Energy 197:292–302. https://doi.org/10.1016/j.apenergy.2017.04.019

Zhang X, Yang J (2015) Power capture performance of an oscillating-body WEC with nonlinear snap through PTO systems in irregular waves. Appl Ocean Res 52:261–273. https://doi.org/10.1016/j.apor.2015.06.012

Zhang X, Yang J, Xiao L (2014) Numerical study of an oscillating wave energy converter with nonlinear snap-through Power-Take-Off systems in regular waves. J Ocean Wind Energy 1:225–230

Zhang X, Tian X, Xiao L, Li X, Chen L (2018) Application of an adaptive bistable power capture mechanism to a point absorber wave energy converter. Appl Energy 228:450–467. https://doi.org/10.1016/j.apenergy.2018.06.100

Zhang X, Tian X, Xiao L, Li X, Lu W (2019a) Mechanism and sensitivity for broadband energy harvesting of an adaptive bistable point absorber wave energy converter. Energy 188:115984. https://doi.org/10.1016/j.energy.2019.115984

Zhang H, Xi R, Xu D, Wang K, Shi Q, Zhao H, Wu B (2019b) Efficiency enhancement of a point wave energy converter with a magnetic bistable mechanism. Energy 181:1152–1165. https://doi.org/10.1016/j.energy.2019.06.008